Interference, Coupling, and Nonlinear Control of High-Order Modes in Single Asymmetric Nanoantennas

Martina Abb,[†] Yudong Wang,[‡] Pablo Albella,[§] C. H. de Groot,[‡] Javier Aizpurua,[§] and Otto L. Muskens[†,*]
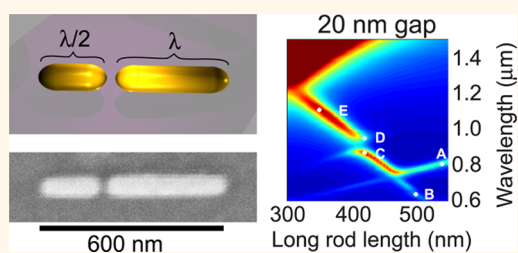
[†]SEPnet and Physics and Astronomy and [‡]Electronics and Computer Science, Faculty of Physical and Applied Sciences, University of Southampton, Highfield, Southampton SO17 1BJ, United Kingdom and [§]Donostia International Physics Center, DIPC, and Centro de Fisica de Materiales, CSIC-UPV/EHU, Paseo Manuel Lardizabal 4, Donostia-San Sebastian 20018, Spain

In recent years, there have been tremendous advances in the design and fabrication of new types of nanoscale optical elements displaying surface plasmon resonances. Plasmonic devices have been very successful in a wide range of applications, including surface-enhanced Raman[1,2] and biosensing for healthcare, near-field optical spectroscopy,[3,4] enhancement of light emission[5,6] and photodetectors,[7,8] and plasmonic metamaterials.[9,10] Analogous to radiowave antennas, plasmonic nanoantennas are designed to efficiently convert optical radiation into a nanometer-sized volume.[11] Plasmonics holds promise as a new paradigm for achieving truly nanoscale, ultrafast optical devices in integrated photonic circuits.[12−14] Active control of the properties of electromagnetic resonances in nanoantennas is generally considered as an important landmark toward the development of transistor-type nanodevices capable of manipulating the flow and emission of light.

In addition to standard dipole gap antennas, many new antenna designs have been developed in recent years to optimize specific properties such as directivity and bandwidth, for example, bowtie antennas, multiparticle clusters supporting Fano-type resonances,[15,16] or 3D, layered antenna designs.[17] These more complex designs also offer new routes for nonlinear control beyond the standard symmetric dimer structures because of the appearance of narrower spectral features associated with nonradiative plasmon modes or, generally, a more intricate dependence of the mode spectrum on the nanoscale geometry.[18]

Recently, a simple new model system has been proposed theoretically based on the coupling between two nanorods of different length.[19−21] Some effects of symmetry breaking have been investigated experimentally in

ABSTRACT

We investigate theoretically and experimentally the structure of plasmonic modes in individual asymmetric dimer antennas. Plasmonic near-field coupling of high-order modes results in hybridization of bright and dark modes of the individual nanorods, leading to an anticrossing of the coupled resonances. For two bright modes, hybridization results in a capacitive red shift and super-radiant broadening. We show that the properties of asymmetric dimers can be used for nonlinear control of spectral modes and demonstrate such a nonlinear effect by measuring the modulation of a hybrid asymmetric dimer—ITO antenna. With use of full electrodynamical calculations, we find that the properties of the near-field nonlinear responses are distinctly different from the far-field, which opens up new routes for nonlinear control of plasmonic nanosystems.

KEYWORDS: plasmon · nanoantenna · asymmetric dimer · Fano resonance · nonlinear response · figure of merit
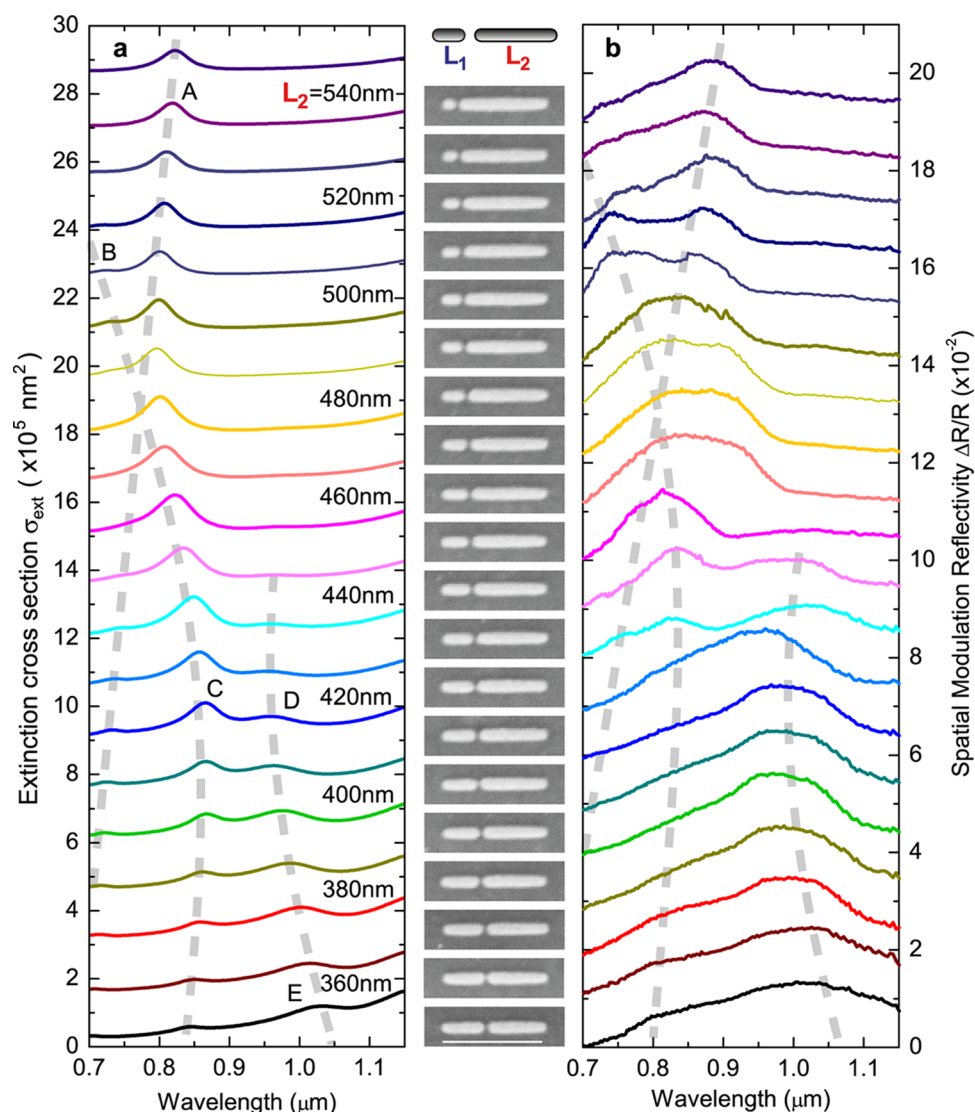
colloidal nanoparticle heterodimers consisting of different sized nanorods and nanospheres.[22−24] As an extension of the highly successful dimer gap antenna concept, asymmetric dimers may be of interest for a variety of applications, such as sum-frequency generation, multifrequency sensors, and Raman scattering.[25−27] Here, we present a combined experimental and theoretical study to address the optical response of individual asymmetric dimers in both the linear and nonlinear regime. Comparison of experimental and calculated spectra confirms the interference and coupling of higher-order plasmonic modes in the nanorods,[28−32] providing evidence of the
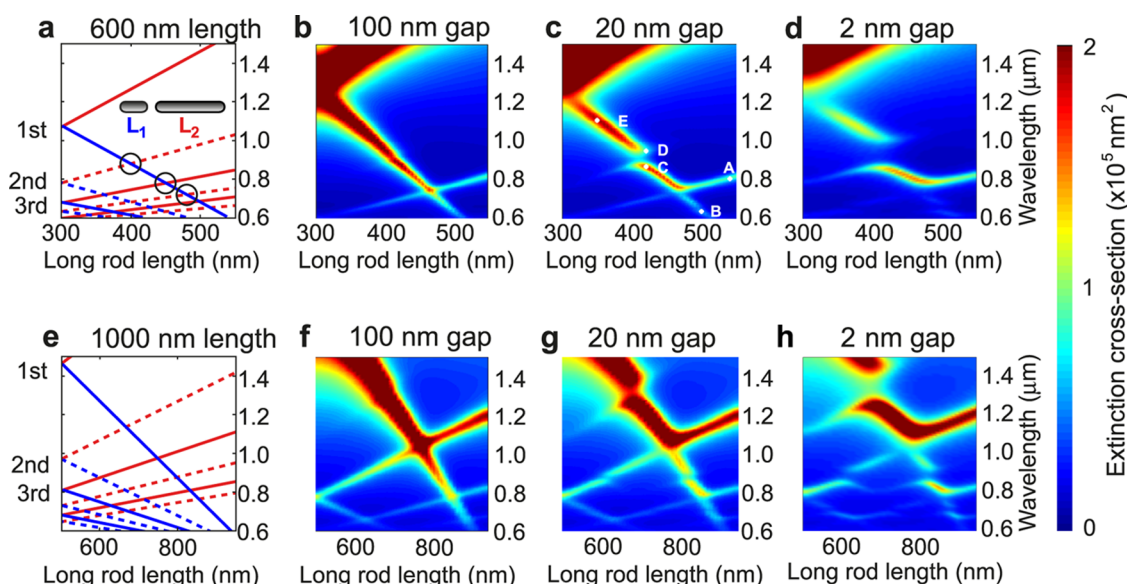
© XXXX American Chemical Society

Figure 1. Theoretical (a) and experimental (b) extinction spectra of individual asymmetric antennas composed of metallic rods of different length L_1 (short rod) and L_2 (long rod). Corresponding SEM images are shown in the center (scale bar, 600 nm). The antennas are separated by a 20 nm gap; *i.e.*, they are in an efficient coupling regime. The total length of both antenna arms is kept constant at $L_{tot} = 600$ nm excluding the gap. The length of the long rod L_2 varies from 360 nm (bottom) to 540 nm (top), with the length of the short rod L_1 decreasing accordingly, as observed in the SEM pictures. A set of surface modes labeled from A to E are identified in the theoretical spectra. Dashed lines are guides of the modes for the eye.

existence of two types of coupling depending on the radiative nature of the modes.

RESULTS AND DISCUSSION

Experimental Spectra of Single Antennas. Figure 1 (center) shows scanning electron microscopy images of selected asymmetric dimer antennas with a gap of 20 nm. The antennas consist of a short (L_1) and a long (L_2) nanorod arm. The length of the long nanorod arm (L_2) is varied from 360 to 550 nm in steps of 10 nm. Extinction spectra of the individual asymmetric dimer antennas are shown in panel b of Figure 1, with corresponding calculations shown in panel a. The spectra show a pronounced dependence on the degree of asymmetry, with good agreement between simulations and experiment. Dashed lines are guides for the eye,

and the different labels from A to E mark points of reference in the spectra for easy comparison with calculations presented further below (Figure 2). We can identify the spectral peaks B and E as corresponding to the fundamental dipole mode of the short rod ($L_1 = \lambda_{eff}/2$, with λ_{eff} being the effective resonance wavelength[28]). As L_1 decreases, L_2 increases in length, producing a red shift of the resonance from B to E. At a length of $L_2 \approx 420$ nm, the dipole mode splits into two branches (marked by points C and D in the graph). For $L_2 = 460$ nm, another crossing of modes is observed without splitting. The fundamental dipole mode for the long antenna ($L_2 = \lambda_{eff}/2$) is located at a longer wavelength, that is, outside of our experimental window. However, we can identify the spectral peak at point A as corresponding to a higher-order bright mode of the long antenna ($L_2 = 3\lambda_{eff}/2$).

Figure 2. (a−d) Spectral position of the resonances for an asymmetric dimer of total length L_{tot} = 600 nm as estimated from the scaling law by Novotny[33] applied to isolated antennas (a), as well as from full electrodynamical calculations of asymmetric antennas weakly interacting (b), and strongly interacting (c,d). (e−h) Same as (a−d) for a total length of L_{tot} = 1000 nm. The modes of the smaller rod are shown in blue in (a) and (e) and the modes of the longer rod in red. Bright modes are displayed in solid lines, whereas dark modes are displayed in dashed lines.

Figure 1 confirms experimentally that the crossing of higher-order modes of the individual nanorods results in a hybridization of the asymmetric antenna modes. To get a complete picture of the underlying interference and coupling between modes, we numerically investigate the interplay between different multipolar modes as a function of the ratio of the lengths of the two antenna segments (L_1/L_2) using model calculations of the optical response of an asymmetric antenna in vacuum. In our calculations, the antenna dimers are modeled as two cylindrical rods with radius R = 15 nm and hemispherical end caps. The total length, including end caps but excluding the gap, was set to 600 nm as in the experiments. We also calculated the additional case where the antennas show a total rod length of L_{tot} = 1000 nm since this situation reveals the interferences of even higher modes (up to $L_{1,2} = 5\lambda_{eff}/2$).

Modeling of Mode Interactions in Asymmetric Dimers. As a first step toward the modeling of the mode interactions in the asymmetric dimer, we first study the modes of each of the segment rods individually. For an overview of the modes sustained by the individual nanorods, we consider the effective wavelength scaling formula given by Novotny,[33] which in the approximation $L \gg R$ can be expressed as

$$\lambda \approx \left(\frac{\lambda_p \varepsilon_s}{0.12\sqrt{\varepsilon_\infty + 141.04\varepsilon_s}} \right) \cdot \left(\frac{nL}{4\pi R} - 13.74 \right.$$
$$\left. - \frac{0.12}{\varepsilon_s}[\sqrt{\varepsilon_\infty + 141.04\varepsilon_s}] - \frac{2}{\pi} \right) \quad (1)$$

Here $\lambda_p \approx 138$ nm is the plasma wavelength of gold, $\varepsilon_\infty \approx 11$ is the infinite frequency limit of the dielectric function for gold, ε_s is the surrounding medium, n is the

order of the mode, and L is the length of the nanorod including the end caps.

Figure 2a shows the calculated positions for the modes of the individual rods $L = L_1$ (short) and $L = L_2$ (long) constituting the asymmetric dimer for the case where the total length L_{tot} = 600 nm, calculated according to eq 1. We plot in solid lines the radiative modes and in dashed lines the nonradiative modes. Modes are radiative if they have a nonzero net dipole moment; the dipole moment depends on the order of the mode; that is, odd multiples of $\lambda_{eff}/2$ are radiative, and even multiples are nonradiative.[28] The modes corresponding to the rod on the left blue shift as the rod length L_1 is decreased, while those of the rod on the right red shift because of the increase in length L_2. This situation leads to the coexistence of modes that belong to each of the segments of the antenna occurring at the same wavelength, and thus causing interference. Several crossings between the fundamental mode of L_1 and higher-order modes of L_2 are indicated by circles in Figure 2a.
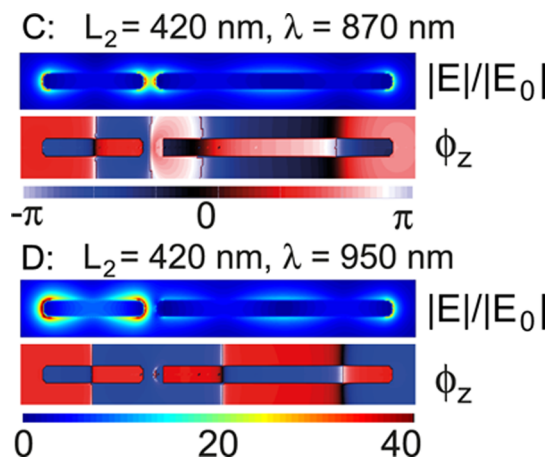
Figure 2a represents the presence of modes in the system, but the actual excitation of each mode is determined by how effectively the external driving field couples to the particular mode. Because of the symmetry, dark modes as the ones represented by the dashed lines in Figure 2a,e are not observed in simulations or in experiments since they cannot be excited using standard plane wave incidence configurations. Also the simple model of eq 1 does not take into account the effect of coupling on the position of the modes but gives a good estimate of the wavelengths where the coupling of modes occurs. The complete effect of the interaction can be unraveled with use of

full electrodynamical calculations. Figure 2b–d shows the results for antennas formed by two asymmetric segments of two different values of the length of the gap between the rods, 100 nm (b), 20 nm (c), and 2 nm (d). For the 100 nm gap, where the interaction is small, the calculations correspond quite well with the expected positions of the individual modes using the simple model. As expected, the dark modes (dashed lines) are not observed in the far-field extinction. Only a small dip is observed around the first crossing point in Figure 2b, which is the first onset of a hybridization between dark and bright modes. This hybridization is observed more clearly in Figure 2c for the case of the dimer with a 20 nm gap. In such a case, the hybridization is pronounced with splitting of modes at length ratios of about $L_1/L_2 \approx$ 1:2 and 1:4. This behavior is observed into greater detail for the nanoantenna with a total length of L_{tot} = 1000 nm, as shown in Figure 2e–h. For the 2 nm gap, the splitting exceeds the line width of the resonances, indicating that the two nanorods are in the strong coupling regime.

To investigate into more detail the induced splitting, we plot both field enhancement and phase of the local near-fields in Figure 3 for modes C and D. Modes C and D are spectrally located at each branch of the mode splitting corresponding to a dimer of total length L_{tot} = 600 nm and long arm length L_2 = 420 nm. The near-field maps clearly show the bonding nature of the mode at 950 nm (mode D), while the mode at 870 nm (mode C) shows an antibonding profile.[34−36] Another feature visible in the phases is the induced charges at the tip of the longer rod caused by the near-field coupling to the bright mode of the short rod.

Strength of Coupling. The strength of the coupling between modes can be tuned by the distance between the two antenna segments, as can be observed in Figure 4a), where we plot the extinction spectrum of the antenna *versus* gap size for an asymmetric antenna. This behavior is confirmed experimentally in Figure 4b, where the splitting of modes is measured in the differential reflectance of asymmetric antennas with different gap sizes of 10, 30, and 40 nm. This splitting corresponds to the avoided crossing of dark and bright modes due to coupling and gives rise to electromagnetically induced transparency (EIT).[37,38] EIT is an effect driven by the interference between excitation pathways that can occur in both quantum and classical oscillator systems. Coupling between a bright and a dark mode results in a near-perfect transparency of the system on an otherwise strong absorption line. The phenomenon is based on the modification of the radiative mode by the presence of a dark, nonradiative mode, which is excited through the near-field coupling with the radiative dipolar mode.
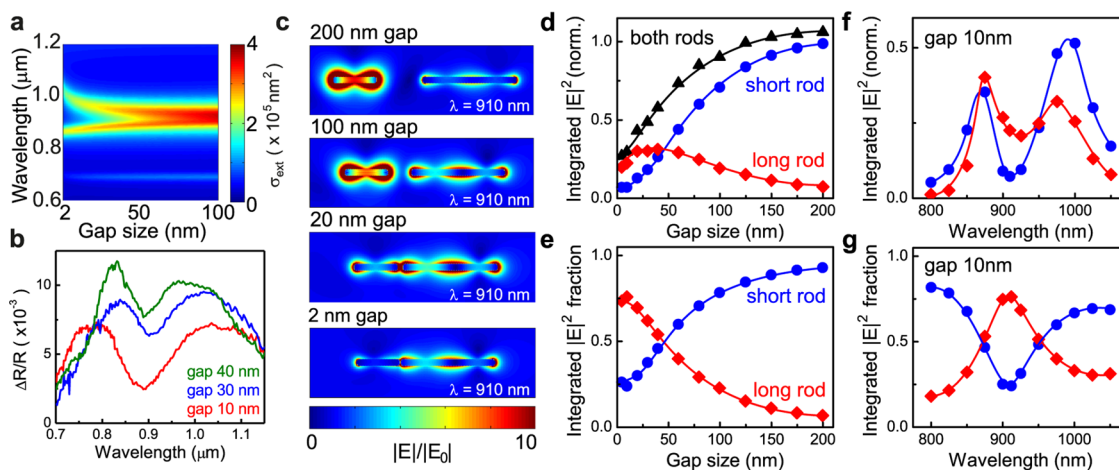
In Figure 4a, we can observe how strongly the EIT splitting is dependent on the dimer separation. In our system, the splitting first occurs at a separation of

Figure 3. Near-field enhancement modulus and phase distribution in the plane perpendicular to the incoming wave at the spectral position of the splitting modes (modes C and D) for L_{tot} = 600 and 20 nm gap.

50 nm. With decreasing separation distances, we see that the splitting becomes asymmetric. The bonding mode red shifts in cubic dependence of the gap size, as expected for dipole−dipole interaction. The antibonding mode, however, blue shifts more slowly. This is caused by the interaction of the plasmon in the shorter nanorod with plasmons of much higher order in the other rod, as already found in the case of spherical nanoparticle dimers.[34] The suppression of the bright mode as a consequence of the coupling with the dark mode is illustrated in Figure 4c, where the near-field distribution around the antenna is represented for decreasing gap sizes from 200 nm down to 2 nm and at a wavelength of 910 nm, that is, in the center of the EIT window. For the large antenna gap, the short nanorod shows a strong dipole mode; however, this mode is almost completely suppressed for a small antenna gap of 2 nm through coupling with the long rod. We estimate the amount of energy transfer from the short rod to the long rod by integrating the square of the near field magnitude |E| in Figure 4c over a contour around each individual rod at a distance of 2 nm away from the edge of the rod. Figure 4d shows the resulting values for the integrated $|E|^2$ for the two rods, normalized to the value for the short rod in absence of the long rod. At large gap sizes, only a small fraction of the mode energy is transferred to the long rod *via* far-field coupling. The integrated $|E|^2$ of the long rod reaches a maximum value for a gap size around 30 nm. This maximum arises because of the combined effect of an increased energy transfer and a suppression of the total mode intensity for small gap sizes, as is illustrated by the black triangles in Figure 4d. In order to assess the relative efficiency of energy transfer from the short rod to the long rod, we also plot in Figure 4e the integrated $|E|^2$ for the two rods normalized to their sum value. This method divides out the variation of the total mode intensity and thus gives a measure of the

Figure 4. (a) Extinction cross section of an asymmetric antenna with $L_2 = 410$ nm and $L_{tot} = 600$ nm as a function of gap size. (b) Experimental spectra of differential reflectance for the same asymmetric antenna for three different gap sizes. (c) Near-field intensity maps at a wavelength of 910 nm (*i.e.*, the center of the EIT window) were calculated for the same length ratio as in (a), with gaps from 200 nm (top) down to 2 nm (bottom). Even at large gaps such as 200 nm, there is still an excitation of the second-order mode of the long nanorod. For very small gap sizes, we observe a suppression of the near-field enhancement in the gap and a stronger excitation of the near-field around the longer rod. (d,e) Integrated local-field intensity $|E|^2$ at 2 nm distance around the short and long rods in the asymmetric dimers of (c) as a function of gap size. (d) Normalized to the total integrated $|E|^2$ of the two rods for infinite gap; (e) same data but normalized to the total integrated $|E|^2$ of the two rods at each gap size. Energy transfer from the bright $\lambda_{eff}/2$ mode of the short rod to the dark λ_{eff} mode of the long rod is observed with up to 76% efficiency. (f,g) Same as (d,e) as a function of wavelength and for a fixed gap size of 10 nm.
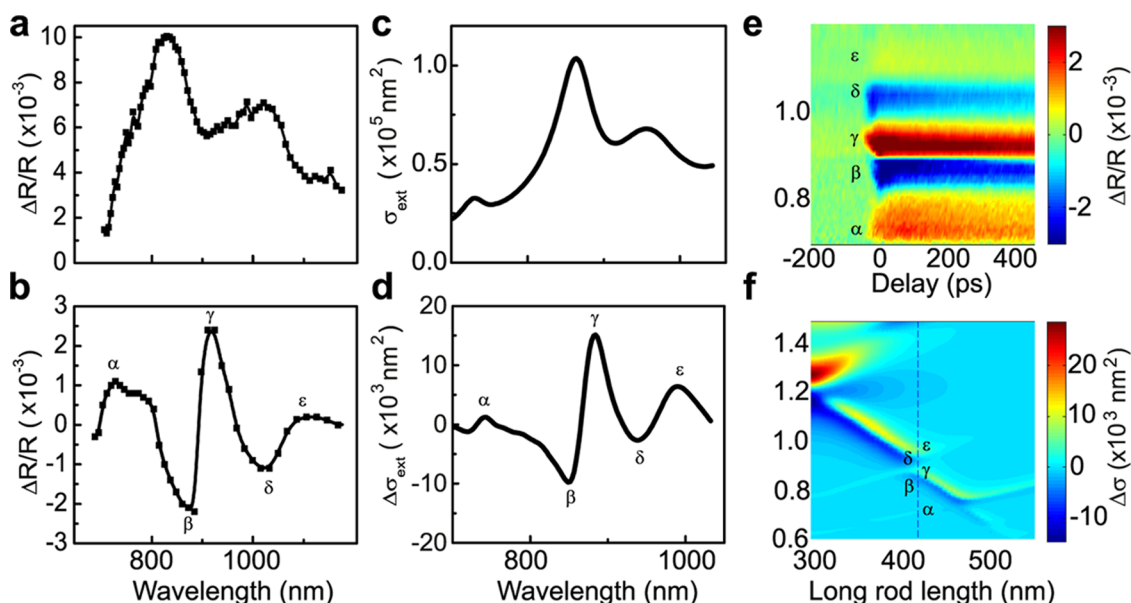
efficiency of energy transfer to the long rod. We find a monotonous increase toward shorter gap sizes in Figure 4e, which levels off for gaps below 10 nm. A maximum transfer efficiency of 76% is found at a gap size of 10 nm. The dependence on wavelength of the integrated $|E|^2$ values, for a fixed gap size of 10 nm, is shown in Figure 4f,g. Indeed, the maximum of energy transfer efficiency to the long rod occurs at 910 nm wavelength, that is, the center of the EIT window of Figure 4a.

On the other hand, crossing of two bright modes does not result in a splitting, as in EIT. Instead, the coherent superposition of two bright modes results in a capacitive red shift and a super-radiant broadening, as can be most clearly observed in the spectra of Figure 1 for $L_2 = 480$ nm. In addition, we find by comparing the efficient coupling case in Figure 2c,d with the weakly coupled case in Figure 2b that the strength of bright modes is significantly affected even away from the crossings. For example, the $3\lambda_{eff}/2$ mode of the long rod (mode A) is significantly suppressed below and enhanced above the crossing with the fundamental $\lambda_{eff}/2$ mode of the short rod (mode B). This suppression as a function of coupling strength is also observed in Figure 4a at the wavelength of 0.7 μm and shows that the short rod couples into the modes of the long rod and *vice versa*, even for configurations where their individual resonances are not spectrally overlapping.

Nonlinear Response of Asymmetric Dimers. We now consider the effect of mode coupling and EIT on the nonlinear response of the asymmetric dimers. We explore the response of an antenna−ITO hybrid

system as a way to achieve a large optical nonlinearity of the combined system,[39] as previously reported for symmetric antennas. The enhancement of the nonlinear response of antenna−ITO hybrids is based on picosecond energy transfer of electronic and thermal excitations generated in the gold antenna by a short pulsed laser excitation. Fast electrons are excited in the gold nanoantenna and injected from the antenna into the ITO. The following thermalization of these electrons leads to heating of the immediate surroundings and subsequent migration of electrons from the heated region. This interaction produces a nonlinear refractive index change of the ITO substrate directly surrounding the antenna, enhancing the hybrid antenna−ITO nonlinear response.

We experimentally investigated the nonlinear response of an asymmetric dimer antenna with long rod length $L_2 = 420$ nm. The differential reflectance corresponding to extinction obtained through the spatial modulation method is shown in Figure 5a, showing the EIT crossing of the modes C and D from Figure 1. The fast picosecond component of the nonlinear modulation signal (*i.e.*, after subtraction of a thermal background) is shown in Figure 5b for a delay of 5 ps between the arrival of pump and probe pulses. The fast transient modulation has a typical decay time of 200 ps given by the cooling dynamics of the substrate.[40] We can observe this time evolution of the nonlinear response at different wavelengths in Figure 5e. In symmetric antennas, a red shift of the dipolar resonance was previously found resulting from a reduction in the free carrier density of the ITO substrate.[39] In our case, the response of the asymmetric dimer shows at
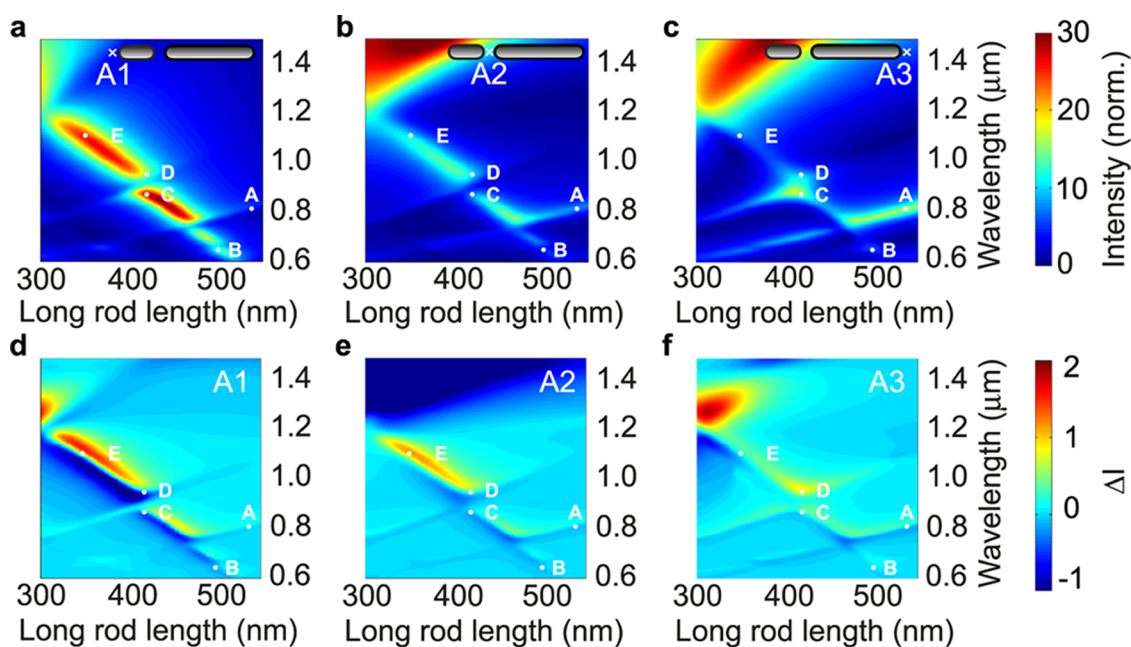
Figure 5. (a) Experimental spectra of differential reflectance $\Delta R/R$ acquired by spatial modulation spectroscopy for a dimer with interference between the first-order mode of the shorter rod segment and the second-order mode of the longer rod segment. (b) Corresponding nonlinear signal for pumping energy of 60 pJ probed with a second pulse at 5 ps delay after the pump pulse arrives, showing the complex dynamics taking place. Symbols $\alpha-\varepsilon$ mark the spectral maxima and minima in the nonlinear response for comparison between experiment and theory. (c,d) Corresponding spectra obtained with FDTD simulations. In (d), the spectrum represented is the differential extinction cross section for a variation of $\Delta N = -6 \times 10^{19}$ cm^{-3} in free carrier density in the ITO. (e) Experimental time-resolved trace of the nonlinear signal. (f) Difference in extinction cross section for an asymmetric dimer of varying lengths using BEM simulations for the same change of free carrier concentrations in the ITO.

least three positive and two negative contributions as marked by the Greek symbols α to ε. Comparison with the numerical model in Figure 5c,d confirms this trend around the EIT anticrossing, showing a red shift for each arm of the splitting. For this calculation, we used an initial free carrier concentration of $N_0 = 7.3 \times 10^{20}$ cm^{-3} in the ITO and an induced change in carrier concentration of $\Delta N = -6 \times 10^{19}$ cm^{-3}, consistent with our earlier findings.[39] The BEM calculation of the differential extinction cross section is shown in Figure 5f and exhibits the same structure of four contributions to the spectrum for the exact situation where the splitting occurs ($L_2 = 420$ nm). This effect can be associated with the red shift of both the upper and lower branches of the hybridized modes. For these BEM calculations, we used a geometry where ITO was present only in the antenna gap; however, the exact distribution of material around the antenna does not strongly influence the behavior for small changes in the free carrier concentration ΔN.[39]

Nonlinearity in the Near-Field. While the far-field shows a nonlinear response characterized by an overall red shift of the resonance spectrum, a more complex behavior is found for the near-field. In Figure 6, we plot the calculated near-field distribution in the proximity of asymmetric antennas at different positions: at 5 nm to the left of the short rod tip (A1), at the midgap (A2), and at 5 nm to the right of the long rod tip (A3). The maps of A1 and A3 are governed by the modes of the short and long rods, respectively, away from the

crossing points. It can be observed in these maps of the local field that, for the lengths where EIT is produced due to the crossing of bright and dark modes, the electromagnetic energy is transferred from the tip of the short rod (A1) to the long rod (A3) (see the bright spots in Figure 6c, coinciding with the dark spots in Figure 6a). This effect can be of interest in many applications. It would be possible, for example, to position a molecule at the end point of the long antenna (A3) which will only be excited through coupling of the long rod with the bright mode of the short rod at the EIT condition. As is shown in Figure 4e, the efficiency of energy transfer can reach 76%; however, the maximum near-field enhancement achieved in A3 is less than that of the short arm dipole in A1, most prominently because of the difference in antenna length and the concomitantly larger mode volume.
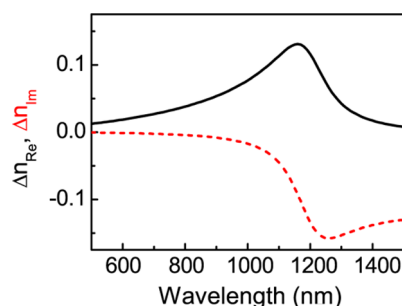
The nonlinear response of the local field intensity, ΔI, is shown in Figure 6d−f for positions A1−A3. Here, ΔI is defined as the difference of the intensity maps calculated using the modified free carrier density $N = 6.7 \times 10^{20}$ cm^{-3} compared with those at the original carrier density N_0. The response above 1.2 μm is associated with the dipole mode of the long antenna outside our spectral window and will not be discussed. Signatures of the red shift as found in the far-field cross section are observed at all three positions. Position A3, however, shows additional effects which cannot be explained by an overall nonlinear shift of the resonance wavelength, but which indicate the presence of other

Figure 6. (a–c) Calculated near-field intensity maps, for a coupled dimer antenna of $L_{tot} = 600$ nm and gap width of 20 nm, as a function of the long arm length L_2. Maps were taken at three positions, respectively, at a distance of 5 nm from the short tip end (A1), in the center of the gap (A2), and at 5 nm from the long rod of the dimer (A3). (d–f) Nonlinear change in near-field intensity $\Delta I = I - I_0$ as calculated in the points A1–A3. For the calculations of I and I_0, we used values for the free-electron density of ITO of $N = 6.7 \times 10^{20}$ cm^{-3} and $N_0 = 7.3 \times 10^{20}$ cm^{-3}, respectively.

contributions in the nonlinear response. Particularly around the branches C and D, only positive values are found for ΔI. This positive nonlinear response is the strongest for the bonding mode (D). We attribute this effect to an increased coupling strength induced by the reduction of the refractive index in the antenna gap. It was observed in Figure 4a that the bonding mode depends more strongly on the coupling strength than the antibonding mode, which is consistent with the difference in ΔI for points C and D in Figure 6f. Such a mechanism is of interest as it shows a distinct difference in nonlinear response associated with the EIT mode, which may be further optimized for applications.

Figure of Merit. Various structures supporting EIT and Fano-type resonances have been proposed and used in the recent literature. In the dolmen-type, π, or heptamer-type structures,[16] the combination of dipoles and/or multipoles oscillating in- and out-of-phase results in a cancellation of fields and the appearance of a dark mode. In the asymmetric dimer, the coupling of a true dark mode with another dipole gives rise to the EIT transparency in analogy with molecular systems.[38] Applications in nonlinear control are similar to those in sensing and benefit from a large sensitivity of the spectral mode structure on local changes in configuration and refractive index combined with enhancement of optical near-fields. The figure of merit (FOM) for such applications is defined by the ratio of the plasmon line shift per refractive index unit, normalized to the spectral width, and allows a comparison of the performance of different types of structures.[41] For

Figure 7. Real part (black line) and imaginary part (red dashed line) of the nonlinear refractive index change of ITO used to model the nonlinear pump–probe spectra of Figure 5 and Figure 6. Values are obtained using the Drude model by subtracting refractive index values at free-electron density of ITO of $N = 6.7 \times 10^{20}$ cm^{-3} and $N_0 = 7.3 \times 10^{20}$ cm^{-3}.

small spectral shifts, the FOM is approximately proportional to the differential pump–probe cross section $\Delta\sigma/\sigma$ in the wing of the resonance (assuming a single resonance without background). This equivalence can be seen from the fact that $\Delta\sigma/\sigma = 0.5$ for a resonance shift equal to half the line width. At the maximum marked by γ in Figure 5d, we find a value of $\Delta\sigma/\sigma = 0.2$. The corresponding refractive index change of the ITO matrix used in this calculation of $\Delta n = 0.056 + 0.009i$ at the wavelength of 910 nm is shown in Figure 7. This value results in a FOM of 3.6 at the γ maximum. This FOM value is comparable to that of other EIT structures reported in literature.[41] It should be noted that, according to Figure 4, the width of the EIT dip, and therefore the FOM, depends on the gap size. A larger

gap results in a smaller splitting and thus a higher figure of merit.

CONCLUSIONS

In conclusion, we have investigated both experimentally and theoretically the interference and coupling of electromagnetic modes in asymmetric dimers. Asymmetric dimers are a relatively simple model system for studying effects of electromagnetically induced transparency. Their simplicity of design is of interest as the geometry, in principle, could be achieved using a variety of techniques including both top-down lithography as well as bottom-up fabrication methods such as colloidal chemistry or electrochemical templated growth. This structure thus opens a path for generation of simple structures that allow for manipulation of EIT and control of spectral resonances. In addition to the linear optical response of the asymmetric dimers, we have demonstrated the signature of EIT splitting also in the nonlinear regime through picosecond modulation of the refractive index of the ITO substrate. The high sensitivity of coupled asymmetric nanorod dimers to the dielectric environment is of potential interest for nonlinear devices and plasmon resonance sensors.

METHODS

Modeling. In order to reproduce the experimental situation as accurately as possible, the substrate and the fine details of the rectangular antenna geometry were considered in the full electrodynamical calculations of the optical response. A finite-difference in time domain (FDTD) method was used (Lumerical) to obtain the results for the antennas deposited on the substrate, whereas systematic calculations of the dependence of the coupled resonances on the different antenna parameters were performed for cylindrical metallic rods in the absence of substrate with the use of the boundary element method (BEM).[42]

Materials. In our experiments, asymmetric dimer antennas of 25 nm thickness were fabricated on an ITO-coated glass substrate using e-beam lithography (JEOL JBX-9300FS) at 100 kV and a dose of 650 $\mu C/cm^2$. The width of all of the antennas was kept fixed at 70 nm.

Single-Particle Spectroscopy. Spectra of individual antennas were measured using a pulsed supercontinuum light source (Fianium, 40 MHz, 4 ps) and a spatial modulation microscopy setup following the method introduced in ref 39. The spatial modulation method is based on the detection of a small variation in optical reflection (or transmission) created by periodic displacement of the antenna in the focus of a microscope objective (Mitutoyo 100× NIR, 0.5 NA).[43,44] The modulation signal was detected using a lock-in amplifier and was directly proportional to the extinction cross section of the antenna. To obtain extinction spectra, the optical wavelength was scanned using a double-prism subtractive mode monochromator. For nonlinear pump−probe experiments, we used the same spectroscopy setup in combination with a synchronized ytterbium fiber amplifier, which was frequency doubled to a wavelength of 530 nm.

Conflict of Interest: The authors declare no competing financial interest.

REFERENCES AND NOTES

1. Rodriguez-Lorenzo, L.; Alvarez-Puebla, R. A.; Pastoriza-Santos, I.; Mazzucco, S.; Stephan, O.; Kociak, M.; Liz-Marzan, L. M.; Garcia de Abajo, F. J. Zeptomol Detection through Controlled Ultrasensitive Surface-Enhanced Raman Scattering. *J. Am. Chem. Soc.* **2009**, *131*, 4616–4618.
2. Kneipp, J.; Li, X.; Sherwood, M.; Panne, U.; Kneipp, H.; Stockman, M. I.; Kneipp, K. Gold Nanolenses Generated by Laser Ablation-Efficient Enhancing Structure for Surface Enhanced Raman Scattering Analysis and Sensing. *Anal. Chem.* **2008**, *80*, 4247–4251.
3. Schnell, M.; Garcia-Etxarri, A.; Huber, A. J.; Crozier, K.; Aizpurua, J.; Hillenbrand, R. Controlling the Near-Field Oscillations of Loaded Plasmonic Nanoantennas. *Nat. Photonics* **2009**, *3*, 287–291.
4. Schnell, M.; Garcia-Etxarri, A.; Alkorta, J.; Aizpurua, J.; Hillenbrand, R. Phase-Resolved Mapping of the Near-Field Vector and Polarization State in Nanoscale Antenna Gaps. *Nano Lett.* **2010**, *10*, 3524–3528.
5. Giannini, V.; Fernandez-Dominguez, A. I.; Heck, S. C.; Maier, S. A. Plasmonic Nanoantennas: Fundamentals and Their Use in Controlling the Radiative Properties of Nanoemitters. *Chem. Rev.* **2011**, *111*, 3888–3912.
6. Curto, A. G.; Volpe, G.; Taminiau, T. H.; Kreuzer, M. P.; Quidant, R.; Van Hulst, N. F. Unidirectional Emission of a Quantum Dot Coupled to a Nanoantenna. *Science* **2010**, *329*, 930–933.
7. Knight, M. W.; Sobhani, H.; Nordlander, P.; Halas, N. J. Photodetection with Active Optical Antennas. *Science* **2011**, *332*, 702–704.
8. Tang, L.; Kocabas, S. E.; Latif, S.; Okyay, A. K.; Ly-Gagnon, D.-S.; Saraswat, K. C.; Miller, D. A. B. Nanometre-Scale Germanium Photodetector Enhanced by a Near-Infrared Dipole Antenna. *Nat. Photonics* **2008**, *2*, 226–229.
9. Valentine, J.; Zhang, S.; Zentgraf, T.; Ulin-Avila, E.; Genov, D. A.; Bartal, G.; Zhang, X. Three-Dimensional Optical Metamaterial with a Negative Refractive Index. *Nature* **2008**, *455*, 376–379.
10. Wurtz, G. A.; Pollard, R.; Hendren, W.; Wiederrecht, G. P.; Gosztola, D. J.; Podolskiy, V. A.; Zayats, A. V. Designed Ultrafast Optical Nonlinearity in a Plasmonic Nanorod Metamaterial Enhanced by Nonlocality. *Nat. Nanotechnol.* **2011**, *6*, 107–111.
11. Novotny, L.; van Hulst, N. Antennas for Light. *Nat. Photonics* **2011**, *5*, 83–90.
12. Brongersma, M. L.; Shalaev, V. The Case for Plasmonics. *Science* **2010**, *328*, 440–441.
13. MacDonald, K. F.; Samson, Z. L.; Stockman, M. I.; Zheludev, N. I. Ultrafast Active Plasmonics. *Nat. Photonics* **2009**, *3*, 55–58.
14. Large, N.; Abb, M.; Aizpurua, J.; Muskens, O. L. Photoconductively Loaded Plasmonic Nanoantenna as Building Block for Ultracompact Optical Switches. *Nano Lett.* **2010**, *10*, 1741–1746.
15. Verellen, N.; Sonnefraud, Y.; Sobhani, H.; Hao, F.; Moshchalkov, V. V.; Van Dorpe, P.; Nordlander, P.; Maier, S. A. Fano Resonances in Individual Coherent Plasmonic Nanocavities. *Nano Lett.* **2009**, *9*, 1663–1667.
16. Luk'yanchuk, B.; Zheludev, N. I.; Maier, S. A.; Halas, N. J.; Nordlander, P.; Giessen, H.; Chong, C. T. The Fano Resonance in Plasmonic Nanostructures and Metamaterials. *Nat. Mater.* **2009**, *9*, 707–715.
17. Liu, N.; Hentschel, M.; Weiss, T.; Alivisatos, A. P.; Giessen, H. Three-Dimensional Plasmon Rulers. *Science* **2011**, *332*, 1407–1410.

18. Alonso-Gonzalez, P.; Schnell, M.; Sarriugarte, P.; Sobhani, H.; Wu, C.; Arju, N.; Khanikaev, A.; Casanova, F.; Hueso, L. E.; Nordlander, P.; *et al.* Real-Space Mapping of Fano Interference in Plasmonic Metamolecules. *Nano Lett.* **2011**, *11*, 3922–3926.

19. Yang, Z.-J.; Zhang, Z.-S.; Zhang, L.-H.; Li, Q.-Q.; Hao, Z.-H.; Wang, Q.-Q. Fano Resonances in Dipole−Quadrupole Plasmon Coupling Nanorod Dimers. *Opt. Lett.* **2011**, *36*, 1542–1544.

20. Woo, K. C.; Shao, L.; Chen, H.; Liang, Y.; Wang, J.; Lin, H.-Q. Universal Scaling and Fano Resonance in the Plasmon Coupling between Gold Nanorods. *ACS Nano* **2011**, *5*, 5976–5986.

21. Huang, C.-P.; Yin, X.-G.; Kong, L.-B.; Zhu, Y.-Y. Interactions of Nanorod Particles in the Strong Coupling Regime. *J. Phys. Chem. C* **2010**, *114*, 21123–21131.

22. Brown, L. V.; Sobhani, H.; Lassiter, J. B.; Nordlander, P.; Halas, N. J. Heterodimers: Plasmonic Properties of Mismatched Nanoparticle Pairs. *ACS Nano* **2010**, *4*, 819–832.

23. Slaughter, L. S.; Wu, Y.; Willingham, B. A.; Nordlander, P.; Link, S. Effects of Symmetry Breaking and Conductive Contact on the Plasmon Coupling in Gold Nanorod Dimers. *ACS Nano* **2010**, *4*, 4657–4666.

24. Shao, L.; Fang, C.; Chen, H.; Man, Y. C.; Wang, J.; Lin, H.-Q. Distinct Plasmonic Manifestation on Gold Nanorods Induced by the Spatial Perturbation of Small Gold Nanospheres. *Nano Lett.* **2012**, *12*, 1424–1430.

25. Danckwerts, M.; Novotny, L. Optical Frequency Mixing at Coupled Gold Nanoparticles. *Phys. Rev. Lett.* **2007**, *98*, 026104.

26. Petschulat, J.; Cialla, D.; Janunts, N.; Rockstuhl, C.; Hübner, U.; Möller, R.; Schneidewind, H.; Mattheis, R.; Popp, J.; Tünnermann, A.; *et al.* Doubly Resonant Optical Nanoantenna Arrays for Polarization Resolved Measurements of Surface-Enhanced Raman Scattering. *Opt. Express* **2010**, *18*, 4184–4197.

27. Harutyunyan, H.; Volpe, G.; Quidant, R.; Novotny, L. Enhancing the Nonlinear Optical Response Using Multifrequency Gold-Nanowire Antennas. *Phys. Rev. Lett.* **2012**, *108*, 217403.

28. Aizpurua, J.; Bryant, G. W.; Richter, L. J.; García de Abajo, F. J.; Kelley, B. K.; Mallouk, T. Optical Properties of Coupled Metallic Nanorods for Field-Enhancement Spectroscopy. *Phys. Rev. B* **2005**, *71*, 235420.

29. Bryant, G. W.; García de Abajo, F. J.; Aizpurua, J. Mapping the Plasmon Resonances of Metallic Nanoantennas. *Nano Lett.* **2008**, *8*, 631–636.

30. Payne, E. K.; Shuford, K. L.; Park, S.; Schatz, G. C.; Mirkin, C. A. Multipole Plasmon Resonances in Gold Nanorods. *J. Phys. Chem. B* **2006**, *110*, 2150–2154.

31. Wei, H.; Reyes-Coronado, A.; Nordlander, P.; Aizpurua, J.; Xu, H. Multipolar Plasmon Resonances in Individual Ag Nanorice. *ACS Nano* **2010**, *4*, 2649–2654.

32. Schmidt, M. K.; Mackowski, S.; Aizpurua, J. Control of Single Emitter Radiation by Polarization- and Position-Dependent Activation of Dark Antenna Modes. *Opt. Lett.* **2012**, *37*, 1017–1019.

33. Novotny, L. Effective Wavelength Scaling for Optical Antennas. *Phys. Rev. Lett.* **2007**, *98*, 266802.

34. Nordlander, P.; Oubre, C.; Prodan, E.; Li, K.; Stockman, M. I. Plasmon Hybridization in Nanoparticle Dimers. *Nano Lett.* **2004**, *4*, 899–903.

35. Ye, J.; Van Dorpe, P.; Lagae, L.; Maes, G.; Borghs, G. Observation of Plasmonic Dipolar Anti-bonding Mode in Silver Nanoring Structures. *Nanotechnology* **2009**, *20*, 465203.

36. Park, T.-H.; Nordlander, P. On the Nature of the Bonding and Antibonding Metallic Film and Nanoshell Plasmons. *Chem. Phys. Lett.* **2009**, *472*, 228–231.

37. Zhang, S.; Genov, D. A.; Wang, Y.; Liu, M.; Zhang, X. Plasmon-Induced Transparency in Metamaterials. *Phys. Rev. Lett.* **2008**, *101*, 047401.

38. Liu, N.; Langguth, L.; Weiss, T.; Kästel, J.; Fleischhauer, M.; Pfau, T.; Giessen, H. Plasmonic Analogue of Electromagnetically Induced Transparency at the Drude Damping Limit. *Nat. Mater.* **2009**, *8*, 758–762.

39. Abb, M.; Albella, P.; Aizpurua, J.; Muskens, O. L. All-Optical Control of a Single Plasmonic Nanoantenna−ITO Hybrid. *Nano Lett.* **2011**, *11*, 2457–2463.

40. Juvé, V.; Scardamaglia, M.; Maioli, P.; Crut, A.; Merabia, S.; Joly, L.; Del Fatti, N.; Vallée, F. Cooling Dynamics and Thermal Interface Resistance of Glass-Embedded Metal Nanoparticles. *Phys. Rev. B* **2009**, *80*, 195406.

41. Lassiter, J. B.; Sobhani, H.; Fan, J. A.; Kundu, J.; Capasso, F.; Nordlander, P.; Halas, N. J. Fano Resonances in Plasmonic Nanoclusters: Geometrical and Chemical Tunability. *Nano Lett.* **2010**, *10*, 3184–3189.

42. Garcia de Abajo, F. J.; Howie, A. Relativistic Electron Energy Loss and Electron-Induced Photon Emission in Inhomogeneous Dielectrics. *Phys. Rev. Lett.* **1998**, *80*, 5180–5183.

43. Arbouet, A.; Christofilos, D.; Del Fatti, N.; Vallé, F.; Huntzinger, J. R.; Arnaud, L.; Billaud, P.; Broyer, M. Direct Measurement of the Single-Metal-Cluster Optical Absorption. *Phys. Rev. Lett.* **2004**, *93*, 127401.

44. Muskens, O. L.; Del Fatti, N.; Vallé, F.; Huntzinger, J. R.; Broyer, M. Single Metal Nanoparticle Absorption Spectroscopy and Optical Characterization. *Appl. Phys. Lett.* **2006**, *88*, 063109.